



Electrochemical behaviour and surface conductivity of niobium carbide-modified austenitic stainless steel bipolar plate



Lixia Wang, Juncai Sun*, Bin Kang, Song Li, Shijun Ji, Zhongsheng Wen, Xiaochun Wang

Institute of Materials and Technology, Dalian Maritime University, Dalian 116026, China

HIGHLIGHTS

- Niobium carbide diffusion layer with dense structure is firstly prepared on 304 SS.
- The niobium carbide diffusion modified 304 SS bipolar plates are evaluated.
- Electrochemical results indicate that the niobium carbide diffusion layer has excellent corrosion resistance.
- The niobium carbide diffusion layer exhibits high surface conductivity even after corrosion tests.

ARTICLE INFO

Article history:

Received 24 June 2013

Received in revised form

8 August 2013

Accepted 10 August 2013

Available online 19 August 2013

Keywords:

Proton exchange membrane fuel cell

Corrosion resistance

Bipolar plate

Interfacial contact resistance

Austenitic stainless steel

Niobium carbide

ABSTRACT

A niobium carbide diffusion layer with a cubic NbC phase surface layer ($\sim 6 \mu\text{m}$) and a Nb and C diffusion subsurface layer ($\sim 1 \mu\text{m}$) is fabricated on the surface of AISI 304 stainless steel (304 SS) bipolar plate in a proton exchange membrane fuel cell (PEMFC) using plasma surface diffusion alloying. The electrochemical behaviour of the niobium carbide diffusion-modified 304 SS (Nb–C 304 SS) is investigated in simulated PEMFC environments (0.5 M H_2SO_4 and 2 ppm HF solution at 80 °C). Potentiodynamic, potentiostatic polarisation and electrochemical impedance spectroscopy measurements reveal that the niobium carbide diffusion layer considerably improves the corrosion resistance of 304 SS compared with untreated samples. The corrosion current density of Nb–C 304 SS is maintained at $0.058 \mu\text{A cm}^{-2}$ and $0.051 \mu\text{A cm}^{-2}$ under simulated anodic and cathodic conditions, respectively. The interfacial contact resistance of Nb–C 304 SS is $8.47 \text{ m}\Omega \text{ cm}^2$ at a compaction force of 140 N cm^{-2} , which is significantly lower than that of the untreated sample ($100.98 \text{ m}\Omega \text{ cm}^2$). Moreover, only a minor increase in the ICR of Nb–C 304 SS occurs after 10 h potentiostatic tests in both cathodic and anodic environments.

© 2013 Elsevier B.V. All rights reserved.

1. Introduction

High performance fuel cells have received increasing attention as alternative power sources due to the adverse environmental impact and decreasing reserves of fossil fuels. Unlike internal combustion engines, in which electric energy is produced from thermal and mechanical energy, fuel cells generate electric energy through electrochemical reactions using a combination of fuel and oxidants. As the most important type of fuel cell, the hydrogen fuelled proton exchange membrane fuel cell (PEMFC) is undergoing rapid development as a power source for mobile applications, especially for electric vehicles, due to its high efficiency and power density, low operating temperature and environmentally friendly properties [1–4]. As a multifunctional component of PEMFCs,

bipolar plates play an important role in connecting the anode of one cell to the cathode of the adjacent cell, supporting the cell stack, collecting current and providing a flow channel for fuel and oxidants. Previous reports have demonstrated that bipolar plates account for approximately 60–80% and 29–45% of the total weight and the total cost of the PEMFC stack, respectively [5–7]. Hence, it is necessary to explore light and low-cost bipolar plates to reduce the total cost and mass of PEMFCs and improve their appeal as commercial devices. Table 1 outlines the specific targets established by the U.S. Department of Energy (DOE) to be achieved by 2015 for bipolar plates in PEMFC stacks for automotive applications [8,9].

Stainless steel is widely accepted as one of the leading PEMFC bipolar plate material candidates due to its suitable physical and mechanical properties as well as relatively low cost [10–12]. However, the corrosion resistance of stainless steel is insufficient for successful application in a commercial PEMFC because the bipolar plates are subjected to acidic environments at elevated temperatures for extended periods of time. Some reports revealed

* Corresponding author. Fax: +86 411 84727959.

E-mail address: sunjc@dlmu.edu.cn (J. Sun).

Table 1
U.S. DOE technical targets for bipolar plates set for the year 2015.

DOE technical targets: bipolar plate	
Cost (\$ kW ⁻¹)	3
System weight (kg kW ⁻¹)	<0.4
H ₂ Permeation flux (cm ³ s ⁻¹ cm ⁻²)	<2 × 10 ⁻⁶
Corrosion (μA cm ⁻²)	<1
Electrical conductivity (S cm ⁻¹)	>100
Interfacial contact resistance at 140 N cm ⁻² (mΩ cm ²)	<10
Durability with cycling (h)	>5000
Flexural strength (MPa)	>25

that metal dissolution (in quantities as low as 5–10 ppm) from the metallic bipolar plates can contaminate the membrane electrode and diminish the performance of the PEMFC [13,14]. Moreover, the passive film formed on stainless steel surfaces in PEMFC environments would increase the interfacial contact resistance (ICR) between the bipolar plate and the gas diffusion layer (GDL), reducing the power output of the fuel cell stack. To address both the insufficient corrosion resistance and high surface resistivity of stainless steel, its surface can be modified with a protective coating. Ideally, the protective coating would be stable and impermeable to reactant gases and provide high conductivity as well as good corrosion resistance to withstand the aggressive PEMFC environment. Noble metals such as gold [15] and silver [16] are suitable coating materials due to their high corrosion resistance and high conductivity, but the commercial use of these materials, even in very thin films, is cost-prohibitive. Transition metals and their nitrides (e.g., Nb, Ta, ZrN, CrN, TiN, Ti/TiN, Ti/CrN, Cr/CrN/Cr) have been widely employed as protective layers for stainless steel bipolar plates using surface treatment techniques, including rolling cladding, magnetron sputtering, electroplating, chemical vapour deposition (CVD) and physical vapour deposition (PVD) [17–25]. Like nitrides, transition metal carbides also possess pronounced physical and chemical properties, such as superconductivity, high hardness, high melting points, high electrical conductivity and good corrosion resistance, making them ideal materials for use as wear resistance and corrosion resistance coatings, field emitters and diffusion barriers [26–31]. In particular, niobium carbide, as a refractory ceramic, exhibits excellent chemical stability and high conductivity. It was reported that niobium carbide exhibits a much higher electrical conductivity than ZrC and TiC [32–35]. Considering these advantageous properties, it is anticipated that niobium carbide may be a suitable protective coating for bipolar plates. However, no prior studies have explored the application of niobium carbide as a coating on bipolar plates. Therefore, in this study, a niobium carbide diffusion layer prepared by plasma surface diffusion alloying was applied as protective layer on an AISI 304 stainless steel (304 SS) bipolar plate. The electrochemical properties and surface conductivity of 304 SS with a niobium carbide diffusion layer (denoted as Nb–C 304 SS hereafter) were investigated in simulated PEMFC environments.

2. Experimental

Commercial austenitic AISI 304 SS sheets with thicknesses of 1.5 mm were employed as the substrate material. The composition of 304 SS is 0.049 C, 18.20 Cr, 8.66 Ni, 0.58 Si, 0.007 S and 0.021 P (wt.%), with the balance comprising Fe. The niobium carbide diffusion layer on the 304 SS sheet was prepared in a double glow plasma alloying furnace using a high purity Nb sinter plate as the sputtering source electrode, the 304 SS samples as the negative cathode and the furnace as the anode. The surface of the substrate was cleaned and heated using argon ion bombardment in a

vacuum chamber filled with pure Ar at a pressure of 40 Pa and a bias voltage of –1 kV. The source electrode power supply was loaded and maintained at –800 V while the bias voltage of the samples was decreased to –500 V. The samples were treated at a temperature of 1173 K for 1 h for the niobium diffusion process, and a proportional volume of acetone gas was then introduced into the chamber as a carbon source. Finally, the samples were treated for another 3 h to form the niobium carbide diffusion layer on the surface of 304 SS.

The crystalline structure of the Nb–C 304 SS was verified by X-ray diffraction (XRD). The surface and cross-sectional morphology as well as the thickness of the niobium carbide diffusion layer were analysed using a scanning electron microscope (SEM, JEOL JSM–6360LV) equipped with an Oxford energy-dispersive X-ray analysis spectrometer (EDS) system. The method reported by Wang et al. [36] was used to measure the interfacial contact resistance (ICR) at different compaction forces. The procedure is described in detail in Refs. [11] and [36].

The corrosion properties of Nb–C 304 SS and untreated 304 SS samples (with an area of 1 cm²) were characterised by electrochemical tests, i.e., potentiodynamic, potentiostatic polarisation and electrochemical impedance spectroscopy (EIS). The tests were conducted using a CHI660C electrochemical workstation controlled by a computer. To simulate the aggressive PEMFC operating conditions, the electrochemical tests were performed in a sulphuric acid aqueous solution (0.5 M H₂SO₄ and 2 ppm HF solution at 80 °C) bubbled with either H₂ or air to simulate the anodic or cathodic environment, respectively. The three-electrode system comprising a saturated calomel electrode (SCE, as the reference electrode), a platinum sheet (as the counter electrode) and the samples (as the working electrode) was constructed for the electrochemical measurements. The EIS tests were carried out at open circuit potential in a frequency range from 100 kHz to 0.01 Hz with amplitude of 10 mV. To quantify the dissolved metallic Fe, Ni, Cr, and Nb ions produced in the potentiostatic process, the test solutions (approximately 100 ml for each test) were collected following 10 h potentiostatic tests, respectively. Inductively coupled plasma atomic emission spectrometry (ICP–AES) (Optima 2000 DV) was used to analyse the metallic ions dissolved in the collected solutions.

X-ray photoelectron spectroscopy (XPS) was employed to identify the superficial composition of the Nb–C 304 SS before and after potentiostatic polarisation. The XPS analysis was conducted in a K-Alpha 1063 (Thermo Fisher Scientific) electron spectrometer using an Al Kα source (1486.8 eV) and a hemispherical energy analyser. To obtain information about the chemical composition throughout the depth of the niobium carbide diffusion layer, Nb–C 304 SS samples (before and after potentiostatic tests) were sputtered with argon ions. The sputtering rate was approximately 0.01 nm s⁻¹ for a period of 250 s, and X-ray photoelectron data were collected every 50 s, corresponding to a thickness of approximately 0.5 nm for each recorded layer. In addition, the thickness of the passive film, if present, can be calculated using the chemical state variation of the detected elements.

3. Results and discussion

3.1. Characterisation of the niobium carbide diffusion layer

The crystal structure of the niobium carbide diffusion layer was verified by X-ray diffraction (XRD). The XRD patterns of Nb–C 304 SS are displayed in Fig. 1. As observed in Fig. 1, only the cubic NbC phase (ICDD card no. 38-1364) with a dominant (111) preferred orientation is observed in the XRD pattern of Nb–C 304 SS, and no peaks from the 304 SS substrate were observed because the

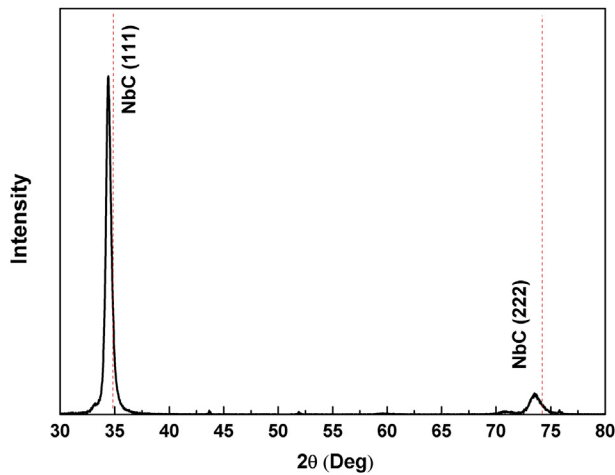


Fig. 1. XRD patterns for Nb–C 304 SS.

penetration depth of the X-ray was less than the thickness of the niobium carbide diffusion layer. It has been reported that niobium carbon binary alloy systems exhibit at least three well-characterised solid carbide phases: a solid solution of carbon in niobium with a body-centred cubic structure, a hemicarbide Nb_2C phase with a hexagonal structure exhibiting good homogeneity within a narrow composition range at room temperature and a monocarbide NbC_x phase with a random face-centred cubic structure, which is homogenous from approximately $\text{NbC}_{0.7}$ to $\text{NbC}_{0.9}$ [37]. As the present XRD pattern indicates, the niobium carbide layer consists of a single cubic NbC phase. As mentioned above, the Nb_2C phase is only observed over a small compositional range in the Nb and C binary phase diagrams, but the single phase NbC forms more readily. Nevertheless, compared with the standard powder diffraction cards (marked by the dash line in Fig. 1), the diffraction peaks from Nb–C 304 SS exhibit shifts to lower angles, which can be ascribed to the compressive stress in the obtained layer [34].

To confirm the composition of the NbC layer, the chemical binding states were analysed by X-ray photoelectron spectroscopy (XPS). Depth profiles of elements in the niobium carbide diffusion layer were obtained by Ar ion sputtering over an area of $1 \times 1 \text{ mm}^2$. High resolution XPS Nb 3d and C 1s spectra were detected every 50 s during the Ar ion sputtering. Fig. 2(a) displays typical Nb 3d spectra from Nb–C 304 SS with and without Ar ion sputtering. An additional peak (210.2 eV) in the Nb 3d spectrum without Ar ion

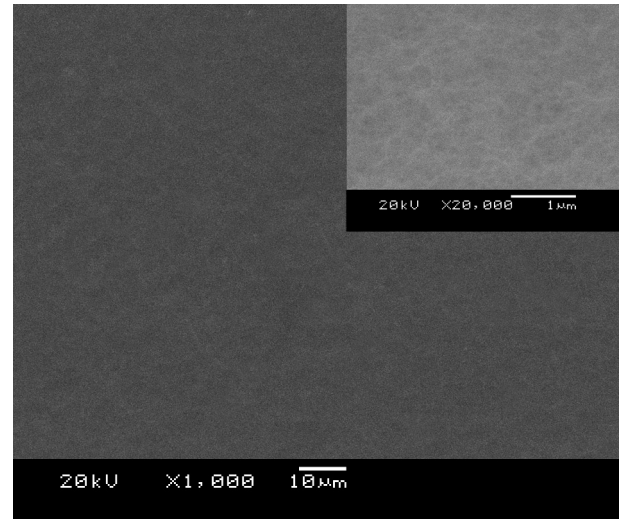


Fig. 3. Surface morphology of Nb–C 304 SS; the insert displays a higher magnification figure.

sputtering is observed due to the adventitious contamination from atmospheric exposure [38]. For the various Ar ion sputtering levels (from 50 s to 250 s), the spectra are similar to each other, with a Nb $3d_{5/2}$ binding energy of approximately 203.6 eV. This binding energy is lower than that of niobium oxides (207.4 eV) and higher than that of pure Nb metal (202.1 eV) and can be assigned to Nb–C binding [38]. Meanwhile, the 282.9 eV binding energy in the C 1s spectra of the various Ar ion sputtering levels (from 50 s to 250 s) (Fig. 2(b)) further confirms the presence of Nb–C binding in the fabricated niobium carbide diffusion layer [39], in agreement with the XRD results displayed in Fig. 1.

The surface morphology of Nb–C 304 SS, as observed by SEM, is displayed in Fig. 3, from which it can be clearly observed that the surface is flat, smooth and compact, without pores or microcracks. Even in the higher magnification image (insert in Fig. 3), the surface appears smooth and continuous, with only subtle surface fluctuations. Fig. 4(a) depicts the cross-sectional SEM morphology of Nb–C 304 SS. As observed in Fig. 4(a), the niobium carbide diffusion layer, with a thickness of approximately 6–7 μm , is uniform, dense and continuous, indicating good metallurgical adhesion to the substrate. No defects, such as pinholes, micropores or microcracks, were observed, suggesting that this modified layer has great potential for use as a protective layer. EDS linear scanning curves of carbon, niobium, nickel, iron and chromium elements were

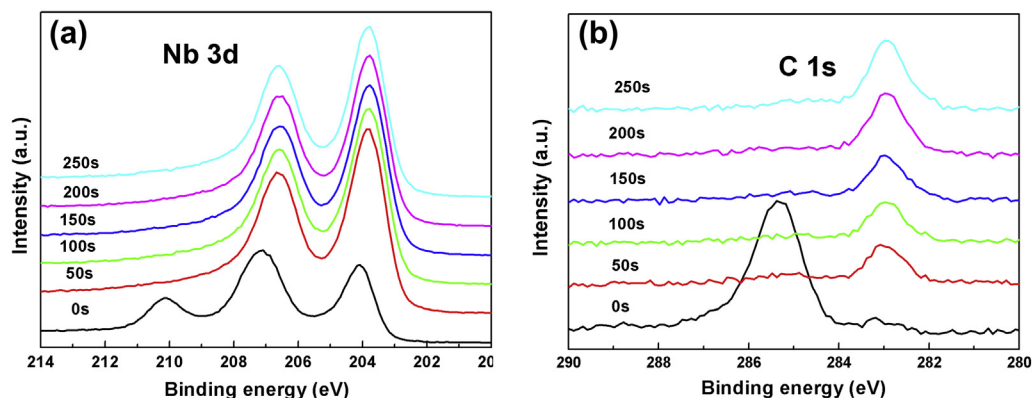


Fig. 2. XPS spectra of Nb 3d (a) and C 1s (b) of Nb–C 304 SS at different Ar ion sputtering levels.

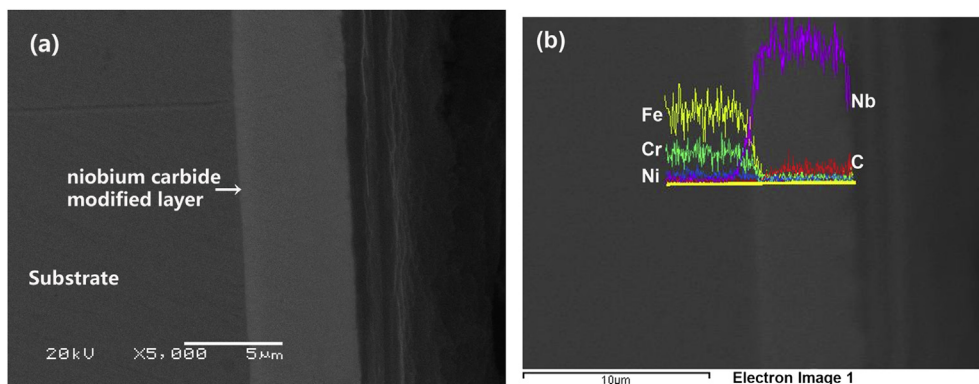


Fig. 4. (a) Cross-sectional view of Nb–C 304 SS; (b) elemental EDS analysis of the niobium carbide diffusion layer.

performed along a short distance across the niobium carbide diffusion layer, as depicted in Fig. 4(b). It can be deduced from the EDS pattern that there exists a niobium carbide surface layer with a thickness of approximately 6 μm and a C and Nb diffusion sub-surface layer (approximately 1 μm in thickness). As we described previously, the formation of niobium carbide diffusion layers is simultaneously affected by both the diffusion and deposition function at high temperatures [11].

3.2. Potentiodynamic polarisation

Good corrosion resistance is one of the most critical requirements for bipolar plate materials in PEMFC stacks. The general corrosion of Nb–C 304 SS and untreated 304 SS samples was investigated using potentiodynamic polarisation. The potentiodynamic polarisation curves of Nb–C 304 SS and untreated 304 SS measured in 0.5 M H_2SO_4 and 2 ppm HF solution at 80 $^\circ\text{C}$ are depicted in Fig. 5(a) (bubbled with H_2 to simulate the anodic environment) and Fig. 5(b) (bubbled with air to simulate the cathodic environment). These results clearly reveal that the polarisation behaviours of untreated 304 SS and Nb–C 304 SS are different from each other. For the untreated samples, the polarisation curves can be divided into five regions both in the simulated cathodic and the simulated anodic environments [12]: in the cathode polarisation region (curve ab), the current density decreases with increasing potential and H_2 evolution is the main electrochemical process; in the anode polarisation region (curve bc), the current density increases with increasing potential and the dissolving of the tested sample is the main electrochemical process; in the active–passive transitional region (curve cd), when the

potential exceeds point c, the current density decreases with increasing potential, and a passive film begins to form on the tested sample surface; in the passive region (curve de), when the potential exceeds point d, the current density stabilises and the passive film covers the entire surface of the tested sample; in the transpassive region (curve ef), the current density increases rapidly with increasing potential once the potential surpasses point e, and the passive film dissolves [7]. However, in contrast to the untreated 304 SS, the potentiodynamic polarisation curves of Nb–C 304 SS in both anodic and cathodic environments exhibit no obvious active–passive transition and can be divided into four regions, namely the cathode region (curve AB), the anode region (curve BC), the passive region (curve CD) and the transpassive region (curve DE), indicating that Nb–C 304 SS can easily achieve a stable state and exhibits improved stability compared with the untreated samples. In addition, the untreated 304 SS displays negative corrosion potentials (E_{corr}) of approximately -0.37 V, while the corrosion potentials of Nb–C 304 SS shift markedly in the positive direction, centred approximately 0.26 V in both the anodic and cathodic environments. Thermodynamically, a higher corrosion potential reflects a higher degree of chemical inertness and better corrosion resistance [7,12].

The corrosion current density (I_{corr}) and E_{corr} can be determined using the linear polarisation method. These results are displayed in Table 2, which reveals that the corrosion current densities of Nb–C 304 SS were far lower than those of the untreated 304 SS. In a simulated anodic environment, the corrosion current density of the untreated sample was $78.370 \mu\text{A cm}^{-2}$, compared with $0.058 \mu\text{A cm}^{-2}$ for Nb–C 304 SS, representing a decrease of more than three orders of magnitude. In the cathodic environment, the

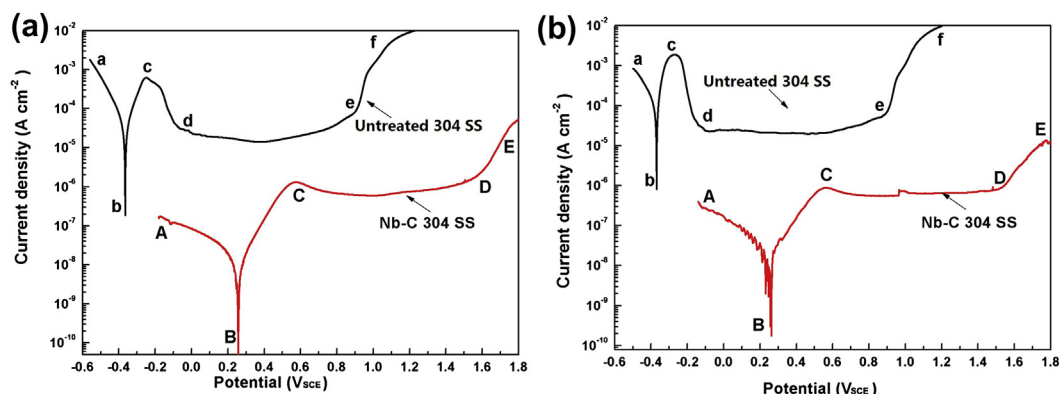


Fig. 5. Potentiodynamic polarisation curves from the untreated 304 SS and Nb–C 304 SS in 0.5 M H_2SO_4 and 2 ppm HF solution at 80 $^\circ\text{C}$ bubbled with H_2 (a) and air (b).

Table 2

The corrosion current density and corrosion potential of samples polarised in simulated PEMFC conditions.

Sample	Anodic environment		Cathodic environment	
	I_{corr} ($\mu\text{A cm}^{-2}$)	E_{corr} (mV)	I_{corr} ($\mu\text{A cm}^{-2}$)	E_{corr} (mV)
Nb–C	0.058	257	0.051	272
Untreated	78.370	–365	319.600	–369

current density of the untreated 304 SS was $319.600 \mu\text{A cm}^{-2}$, while that for Nb–C 304 SS was only $0.051 \mu\text{A cm}^{-2}$, representing a decrease of four orders of magnitude. As revealed by the potentiodynamic results, the corrosion current densities of the untreated 304 SS were remarkably high, preventing their use as PEMFC bipolar plates. In contrast, Nb–C 304 SS exhibited a significant decrease in the corrosion current density, surpassing the DOE target for corrosion resistance. Such low corrosion current densities indicate that the corrosion resistance of Nb–C 304 SS is considerably improved compared with untreated 304 SS. Therefore, the dense niobium carbide diffusion layer might protect the substrate well from corrosion in bipolar plate applications.

3.3. Electrochemical impedance spectroscopy

Electrochemical impedance spectroscopy (EIS) is an effective method for studying the corrosion processes of electrical conductors in electrolytes because of the low amplitude of its perturbation signal, which allows the monitoring of the electrode electrochemical behaviour with time without altering its surface properties. Fig. 6 presents the Nyquist plots for the untreated samples and Nb–C 304 SS acquired under simulated cathodic PEMFC conditions after a 1 h immersion at OCP. Within the frequency range of the measurement, the Nyquist plots for Nb–C 304 SS display one depressed semicircle, while those for the untreated 304 SS present a high frequency semicircle and a low frequency Warburg diffusion tail. Therefore, the impedance spectra were analysed using two different equivalent circuit models, as illustrated in Fig. 7(a) for Nb–C 304 SS and (b) for untreated 304 SS, where R_s denotes the solution resistance between the reference and working electrode; R_c and C_{dl} denote the charge transfer resistance and double layer capacitance, respectively; R_f and C_f denote the resistance and capacitance of the porous corrosion product layer [40,41], respectively and W denotes the Warburg impedance. Due to the non-ideal capacitive response of the interface between the sample and

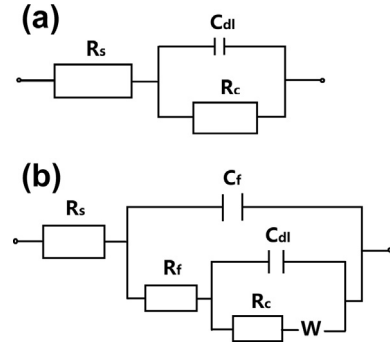


Fig. 7. Equivalent circuits of the corrosion system for (a) the Nb–C 304 SS/solution; (b) the untreated 304 SS/solution.

solution, a constant phase element (CPE) was introduced to replace both C_{dl} and C_f in the fitting procedure. The impedance of the CPE can be represented as:

$$Z_{\text{CPE}} = 1/Q(j\omega)^n \quad (1)$$

where Q is the admittance magnitude of CPE, ω is the angular frequency and n is the exponential term. When $n = 1$, Z_{CPE} is equal to the pure capacitance impedance. The pure resistor impedance is represented by $n = 0$. Practically, n is in the range between 0 and 1, and Q can be approximated by the capacitance [42,43]. It can be observed in Fig. 6 that the physical models provided accurate fits to the experimental data, especially with respect to the shape of the impedance spectra in the Nyquist plots. Therefore, it was concluded that the models provided a reliable representation of the corrosion system. The fitted results are summarised in Table 3. The solution resistances (R_s) of the two samples were nearly equal in value, suggesting a similar ion conductivity in the test solutions. The charge transfer resistance for Nb–C 304 SS was $1.927 \times 10^6 \Omega \text{ cm}^2$, two orders of magnitude higher than that for untreated 304 SS ($1.996 \times 10^4 \Omega \text{ cm}^2$). The higher charge transfer resistance reflects a lower corrosion rate.

3.4. Potentiodynamic polarisation

The stability of Nb–C 304 SS was investigated using potentiostatic tests in simulated PEMFC environments for 10 h. Fig. 8(a) displays the current density vs. time results for Nb–C 304 SS and the untreated samples under an applied potential of $0.6 V_{\text{SCE}}$ with air bubbling. The current density of the untreated 304 SS was initially high and decayed rapidly with time, then stabilised gradually at a low value, while the potentiostatic polarisation curve for Nb–C 304 SS exhibited static values over the same time range. The current density of Nb–C 304 SS was far lower than that of the untreated sample throughout the potentiostatic test, as depicted in the inset in Fig. 8(a). The current density of Nb–C 304 SS exhibited the same transition trend as that of untreated 304 SS, although in a lower value range. The variations in the current density of the test samples can be attributed to the formation of a protective, passive film [17–22]: in the initial stage of the test, a passive film forms and the current density begins to drop; once the passive film covers the entire surface of the sample, the current density maintaining the passive film decreases dramatically. The current density finally stabilised at $(7\text{--}8) \mu\text{A cm}^{-2}$ for the untreated 304 SS and at $0.02 \mu\text{A cm}^{-2}$ for Nb–C 304 SS, a reduction of over two orders of magnitude. Generally, a current density as low as that observed for Nb–C 304 SS indicates fewer electrochemical reactions occurring on the interface and in the adjacent electrolytes as well as

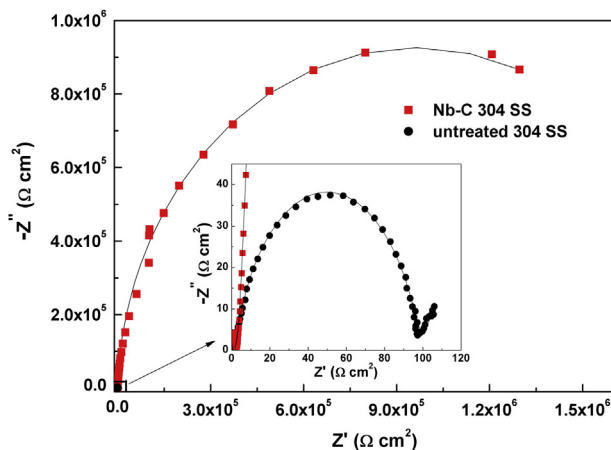


Fig. 6. Nyquist plots from the untreated 304 SS and Nb–C 304 SS measured by EIS in a simulated cathodic PEMFC environment.

Table 3

Fitted results of EIS spectra for untreated and Nb–C 304 SS.

Sample	Circuit model	R_s (Ω cm ²)	Q_{dl} (Ω^{-1} cm ⁻² s ⁻ⁿ)	R_c (Ω cm ²)	n_{dl}	Q_r (Ω^{-1} cm ⁻² s ⁻ⁿ)	n_r	R_f (Ω cm ²)	W (Ω^{-1} s ^{-0.5} cm ⁻²)
Untreated	a	1.767	0.2834	1.996×10^4	0.8561	2.427×10^{-4}	0.5292	95.82	9.093×10^{-8}
Nb–C	b	1.801	3.09×10^{-4}	1.927×10^6	0.8748	—	—	—	—

diminished metal ion release in solution relative to the untreated 304 SS. The actual quantity of released metal ions in solution is discussed in subsequent sections. Fig. 8(b) displays the potentiostatic polarisation curves for Nb–C 304 SS and untreated 304 SS at -0.1 V_{SCE} in an anodic environment. Similarly, the current density of Nb–C 304 SS is significantly lower than that of the untreated sample, as revealed in the inset in Fig. 8(b). The behaviour of the untreated 304 SS in the anodic environment was similar to its behaviour in the cathodic environment, with the current density dropping dramatically and then gradually stabilising at a relatively low value (approximately $8 \mu\text{A cm}^{-2}$). However, the current density of Nb–C 304 SS remained negative throughout the potentiostatic test in the anodic environment and finally stabilised at approximately $-0.05 \mu\text{A cm}^{-2}$. The negative current density can be attributed to the nobler corrosion potential of Nb–C 304 SS relative to the anode potential (-0.1 V_{SCE}), which causes the reduction of H⁺ ions to H₂ [12]. In addition, this negative current density can provide cathodic protection for Nb–C 304 SS.

Metal ions produced from corrosion in solution not only lead to a decrease in membrane conductivity due to their higher affinity for sulphuric acid than H⁺ but also cause the poisoning of the electrode catalysts [44], resulting in severe performance degradation in the PEMFC stack. Therefore, it is necessary to quantify the metal ions released by electrochemical corrosion to gauge the performance of the metallic bipolar plate materials. The concentration of dissolved metal ions in H₂SO₄ and HF solutions was detected by ICP-AES after 10 h potentiostatic polarisation tests. A considerable amount of metal ions were detected in the test solutions from the untreated 304 SS samples both in anodic (Fe: 10.0281 ppm, Cr: 0.9914 ppm, Ni: 0.7106 ppm) and cathodic (Fe: 7.6152 ppm, Cr: 0.9467 ppm, Ni: 0.8288 ppm) environments. However, no detectable levels of metal ions were dissolved in the test solutions from Nb–C 304 SS after 10 h potentiostatic tests in either the cathodic or anodic environments, demonstrating the superior corrosion resistance of the niobium carbide diffusion layer.

3.5. XPS analysis

Fig. 9 presents the XPS results from Nb–C 304 SS following the potentiostatic tests in the cathodic environment. The results from

the anodic environment were similar and therefore are not shown. Fig. 9(a) presents the high resolution XPS spectra of Nb 3d with and without Ar ion sputtering. After the first 50 s Ar sputtering, the bonding energy of Nb 3d was approximately 203.6 eV, indicating Nb–C bonding. This result was verified by the XPS spectra of C 1s, with a bonding energy of approximately 282.9 eV after the first 50 s Ar ion sputtering, as displayed in Fig. 9(b). The XPS depth profiles of Nb, C and O are depicted in Fig. 9(c). It was observed that the atomic concentration of O decreased to a negligible level after the first 50 s Ar ion sputtering. Because the Ar sputtering rate was approximately 0.01 nm per second, it was inferred that the passive film, if present, was less than 0.5 nm thick. Such a surface state following the potentiostatic tests would improve the surface conductivity, providing low interfacial contact resistance.

3.6. Interfacial contact resistance

The surface conductivity of the bipolar plates can be characterised using interfacial contact resistance (ICR) measurements. The ICR originating from the interface between the gas diffusion layer and the bipolar plate exerts a dramatic effect on the PEMFC stack efficiency. It was reported that increases in ICR result in power losses on the order of 2–5% per 25 mV (per cm²) compared with graphite plates [22]. In addition, the cost of a PEMFC stack (per kW) is estimated to increase three-fold when the stack resistance increases from 0.05 m Ω cm² to 0.2 m Ω cm² [19]. Therefore, the performance of a PEMFC system can be greatly improved by minimising the ICR. The ICR between the Nb–C 304 SS and the carbon paper before and after the potentiostatic tests was investigated as a function of the compaction force, as described in Fig. 10. The ICR values of the untreated samples were also added for comparison. To better interpret the data points at high compaction forces, a log scale for the ICR was adopted when plotting ICR vs. compaction pressure. The square and hexagonal data points in Fig. 10 reveal the dependence of the ICR (before the corrosion tests) of the untreated and Nb–C 304 SS samples on the compaction force, respectively. Both of the samples exhibited typical ICR behaviour [18–20]: the compaction force acted as the dominant influence on the ICR at low pressures, while the surface composition was the predominant factor at higher compaction forces. The

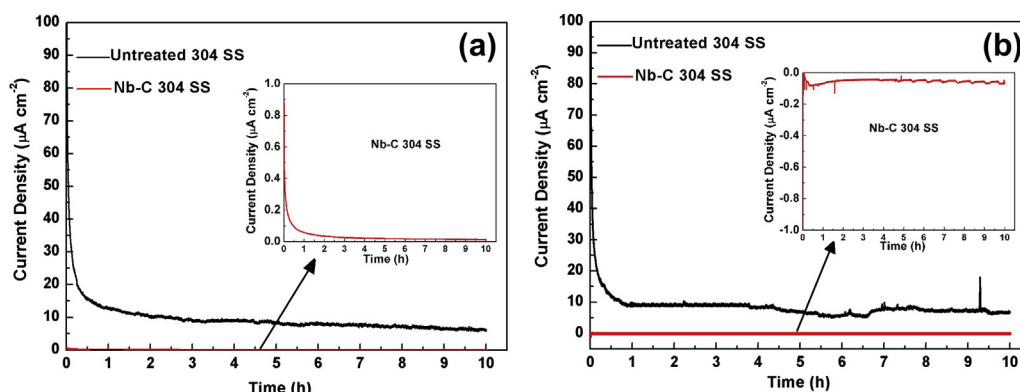


Fig. 8. Current density–time relationship of the untreated 304 SS and Nb–C 304 SS in 0.5 M H₂SO₄ and 2 ppm HF solution at 80 °C bubbled with air (a) and H₂ (b).

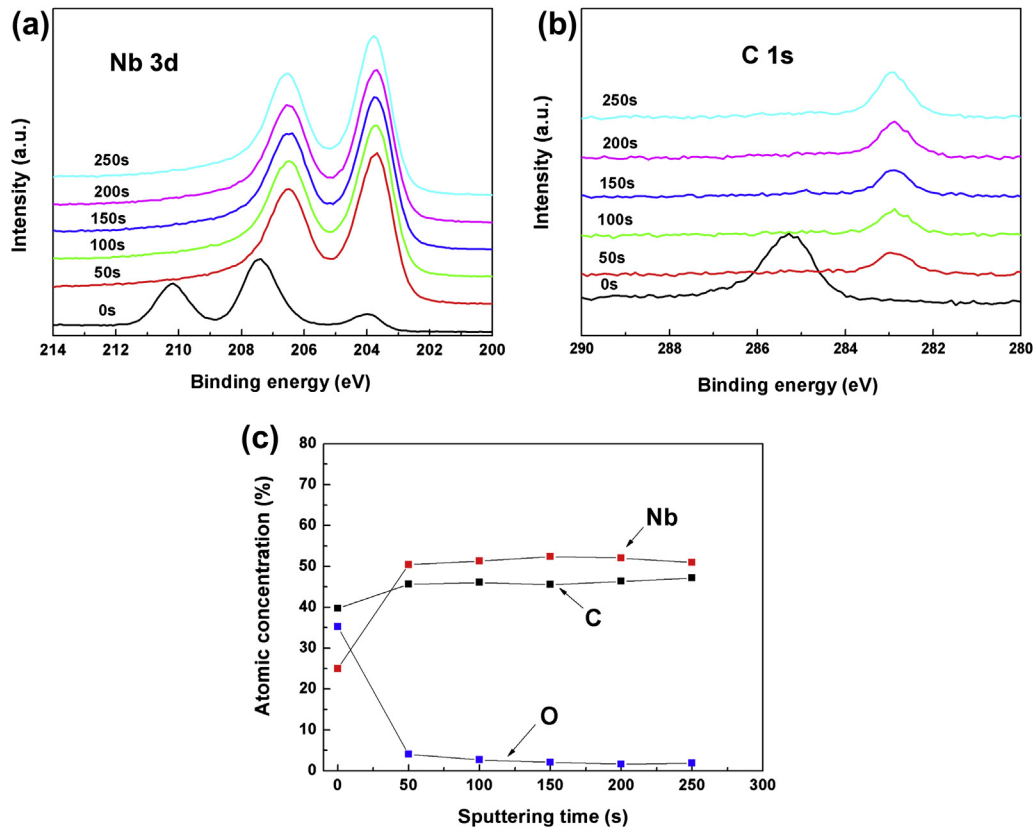


Fig. 9. XPS spectra of Nb 3d (a) and C 1s (b) and the depth profile (c) of Nb–C 304 SS at various Ar ion sputtering levels after 10 h potentiostatic tests in a cathodic environment.

Nb–C 304 SS samples exhibited much lower contact resistance values than the untreated samples due to the natural air-formed oxide layer on the bare stainless steel surface. Under the common applied compaction force of 140 N cm^{-2} (line in Fig. 10), the ICR for the untreated 304 SS was $100.98 \text{ m}\Omega \text{ cm}^2$, while the ICR decreased to $8.47 \text{ m}\Omega \text{ cm}^2$ for Nb–C 304 SS, fulfilling the requirements of the DOE 2015 target of less than $10 \text{ m}\Omega \text{ cm}^2$. As discussed previously, the ICR is primarily influenced by the conductivity of the sample surface at a fixed pressure, which is affected by the nature of the surface materials. In this case, the considerably lower ICR observed for Nb–C 304 SS can be attributed to the good electrical

conductivity of the niobium carbide. In addition, the niobium carbide diffusion layer exhibits superior conductivity compared with niobized layer [5] ($10.53 \text{ m}\Omega \text{ cm}^2$) and niobium nitride layers ($9.26 \text{ m}\Omega \text{ cm}^2$) [11] at compaction forces of 140 N cm^{-2} .

The circular and triangular data points in Fig. 10 represent the ICRs of untreated 304 SS following potentiostatic tests for over 10 h in simulated anodic and cathodic environments, respectively. It has been reported that the air-formed thin oxide film primarily consisting of iron and chromium oxides might not protect the stainless steel from further corrosion under the PEMFC operating conditions [17–21]. A semi-conductive passive film with a predominantly chromium oxide composition will develop and thicken under the PEMFC operating conditions, greatly reducing the surface conductivity of stainless steel. Hence, the ICRs of the untreated samples following the potentiostatic tests increase greatly in comparison with those before the tests both in anodic and cathodic environments. For Nb–C 304 SS, however, the increases in the ICR following the 10 h potentiostatic tests in both anodic (pentastar points in Fig. 10) and cathodic (pentagon points in Fig. 10) environments were so subtle that they were nearly equivalent at the same compaction force. At an applied compaction force of 140 N cm^{-2} , the ICR of Nb–C 304 SS was $8.77 \text{ m}\Omega \text{ cm}^2$ and $9.04 \text{ m}\Omega \text{ cm}^2$ following the anodic and cathodic potentiostatic tests, respectively, and far lower than that for the untreated 304 SS of $183.47 \text{ m}\Omega \text{ cm}^2$ and $285.31 \text{ m}\Omega \text{ cm}^2$, respectively. The XPS analysis following the potentiostatic tests revealed that the surface chemical states of the Nb–C 304 SS were unchanged compared with the as-prepared surface, and the passive film, if present, was less than 0.5 nm thick. During the 10 h potentiostatic tests, the current densities for Nb–C 304 SS (Fig. 8(a) and (b)) were quite low and exhibited no evident fluctuation, indicating that the Nb–C 304 SS was stable in both anodic and cathodic environments. Therefore,

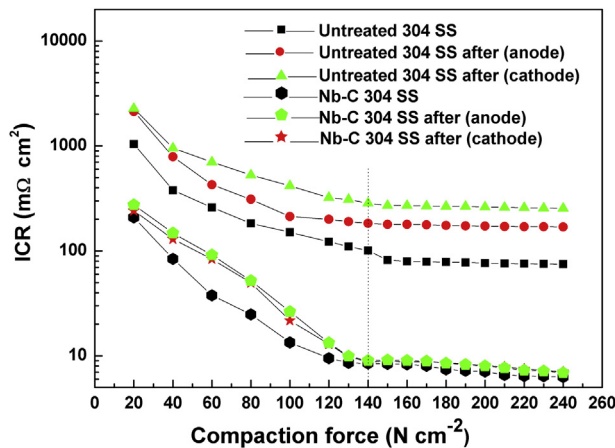


Fig. 10. ICR of untreated 304 SS and Nb–C 304 SS under varying compaction forces before and after the potentiostatic tests in simulated anodic and cathodic environments.

the niobium carbide diffusion layer enabled high conductivity under the PEMFC operating conditions, which could significantly reduce the ohmic loss in PEMFC stacks.

4. Conclusions

A niobium carbide-modified 304 SS bipolar plate was successfully prepared by the plasma surface alloying method. XRD and XPS analyses indicated that a cubic NbC phase was formed. SEM images revealed a dense, uniform, smooth and continuous niobium carbide diffusion layer with a thickness of approximately 6–7 μm that exhibited good metallurgical adhesion to the substrate. The potentiodynamic, potentiostatic polarisation and EIS results provided evidence that the corrosion resistance of the 304 SS substrate was significantly improved by the niobium carbide diffusion layer. The self-corrosion potentials of Nb–C 304 SS increased considerably, rising to 257 mV and 272 mV (vs. SCE), while the corrosion current densities remained low, with values of $0.058 \mu\text{A cm}^{-2}$ and $0.051 \mu\text{A cm}^{-2}$ being observed in simulated anodic and cathodic environments, respectively. Furthermore, Nb–C 304 SS exhibited a charge transfer resistance of $1.927 \times 10^6 \Omega \text{cm}^2$, two orders of magnitude higher than that for untreated 304 SS ($1.996 \times 10^4 \Omega \text{cm}^2$). In addition, following 10 h potentiostatic tests, the niobium carbide diffusion layer was stable and no metal ion dissolution had occurred, as confirmed by ICP-AES. The ICR measurements revealed a superior surface conductivity due to the inherently high electrical conductivity of the NbC. At an applied compaction force of 140 N cm^{-2} , the ICR of Nb–C 304 SS was $8.47 \text{ m}\Omega \text{cm}^2$ and increased to $8.77 \text{ m}\Omega \text{cm}^2$ and $9.04 \text{ m}\Omega \text{cm}^2$ following 10 h potentiostatic tests in anodic and cathodic environments, respectively. The overall performance suggests that the niobium carbide-modified 304 SS bipolar plate developed in this work will exhibit excellent performance in PEMFCs.

Acknowledgements

This work was financially supported by the National Foundation of Natural Science of China (No. 21176034), the Fundamental Research Funds for the Team of Central Universities (No. 3132013314) and the Scientific Research Foundation for National Excellent Doctoral Dissertation Program (No. 2013YB02).

References

- [1] M.Z. Jacobson, W.G. Colella, D.M. Golden, *Science* 308 (2005) 1901–1905.
- [2] C.E. Borroni–Bird, *J. Power Sources* 61 (1996) 33–48.
- [3] S.G. Chalk, J.F. Miller, F.W. Wagner, *J. Power Sources* 86 (2000) 40–45.
- [4] B.D. Cunningham, D.G. Baird, *J. Power Sources* 168 (2007) 418–425.
- [5] L.X. Wang, J.C. Sun, P.B. Li, B. Jing, S. Li, Z.S. Wen, S.J. Ji, *J. Power Sources* 208 (2012) 397–403.
- [6] H. Wang, J.A. Turner, X. Li, R. Bhattacharya, *J. Power Sources* 171 (2007) 567–574.
- [7] H. Yu, L. Yang, L. Zhu, X. Jian, Z. Wang, L. Jiang, *J. Power Sources* 191 (2009) 495–500.
- [8] http://www.hydrogen.energy.gov/pdfs/progress12/v_h_1_wang_2012.pdf.
- [9] W. Yoon, X. Huang, P. Fazzino, K.L. Reifsnider, M.A. Akkai, *J. Power Sources* 179 (2008) 265–273.
- [10] H. Wang, J.A. Turner, *J. Power Sources* 128 (2004) 193–200.
- [11] L.X. Wang, J.C. Sun, J. Sun, Y. Lv, S. Li, S.J. Ji, Z.S. Wen, *J. Power Sources* 199 (2012) 195–200.
- [12] Y. Wang, D.O. Northwood, *J. Power Sources* 163 (2006) 500–508.
- [13] M.P. Brady, K. Weisbrod, I. Paulauskas, R.A. Buchanan, K.L. More, H. Wang, M. Wilson, F. Garzon, L.R. Walker, *Scripta Mater.* 50 (2004) 1017–1022.
- [14] L.X. Wang, J.C. Sun, P.B. Li, J. Sun, Y. Lv, B. Jing, S. Li, S.J. Ji, Z.S. Wen, *Int. J. Hydrogen Energy* 37 (2012) 5876–5883.
- [15] Y. Wang, D.O. Northwood, *J. Power Sources* 175 (2008) 40–48.
- [16] I.B. Huang, *J. Power Sources* 196 (2011) 7649–7653.
- [17] R.C. Makkus, A.H.H. Janssen, F.A. de Bruijn, R.K.A.M. Mallant, *J. Power Sources* 86 (2000) 274–282.
- [18] H. Wang, G. Teeter, J.A. Turner, *J. Electrochem. Soc.* 152 (2005) B99–B104.
- [19] A. Kraysberg, M. Auinat, Y. Ein-Eli, *J. Power Sources* 164 (2007) 697–703.
- [20] R.G. Rajendran, *MRS Bull.* 30 (2005) 587–590.
- [21] R.J. Tian, J.C. Sun, L. Wang, *Int. J. Hydrogen Energy* 31 (2006) 1874–1878.
- [22] A. Heinzl, F. Mahlendorf, O. Niemzig, C. Kreuz, *J. Power Sources* 131 (2004) 35–40.
- [23] R.J. Tian, J.C. Sun, *J. Power Sources* 194 (2009) 981–984.
- [24] R.J. Tian, J.C. Sun, *Int. J. Hydrogen Energy* 36 (2011) 6788–6794.
- [25] R.J. Tian, J.C. Sun, L. Wang, *J. Power Sources* 163 (2007) 719–724.
- [26] Y. Zhang, F. Ronning, K. Gofryk, N.A. Mara, N. Haberkorn, G. Zou, H. Wang, J.H. Lee, E. Bauer, T.M. McCleskey, A.K. Burell, L. Cival, Y.T. Zhu, Q. Jia, *Nanoscale* 4 (2012) 2268–2271.
- [27] S. Ramanathan, S.T. Oyama, *J. Phys. Chem.* 99 (1995) 16365–16372.
- [28] R. Jha, V.P.S. Awana, *J. Supercond. Nov. Magn.* 25 (2012) 1421–1425.
- [29] Y.J. Ren, C.L. Zeng, *J. Power Sources* 171 (2007) 778–782.
- [30] S.R. Vallance, D.M. Round, C. Ritter, E.J. Cussen, S. Kingman, H. Gergory, *Adv. Mater.* 21 (2009) 4502–4504.
- [31] L. Ramqvist, K. Hamrin, G. Johansson, A. Fahlman, C. Nording, *J. Phys. Chem. Solids* 30 (1969) 1835–1847.
- [32] F.W. Clinard, J.R. Kempter, C.P. Kempter, *J. Less-Common Met.* 15 (1968) 59–73.
- [33] B. Sustarsic, M. Jenko, M. Godec, L. Kosec, *Vacuum* 71 (2003) 77–82.
- [34] K. Zhang, M. Wen, Q.N. Meng, C.Q.K. Hu, X. Li, C. Liu, W.T. Zheng, *Surf. Coat. Technol.* 212 (2012) 185–191.
- [35] D.A. Papaconstantopoulos, W.W. Pickett, B.M. Klein, L.L. Boyer, *Phys. Rev. B* 31 (1985) 753–761.
- [36] H. Wang, M.A. Sweikart, J.A. Turner, *J. Power Sources* 115 (2003) 243–251.
- [37] E.K. Storms, N.H. Krikorian, *J. Phys. Chem.* 64 (1960) 1471–1477.
- [38] M.Y. Liao, Y. Goto, H. Tsuji, J. Ishikawa, *J. Vac. Sci. Technol., B* 5 (2004) L24–L27.
- [39] N. Nedfors, O. Tengstrand, E. Lewin, A. Furlan, P. Eklund, L. Hultman, U. Jansson, *Surf. Coat. Technol.* 206 (2011) 354–359.
- [40] K. Juttner, W.J. Loronz, *J. Electrochem. Soc.* 135 (1988) 332–339.
- [41] I. Frateur, C. Deslouis, M.E. Orazem, B. Tribollet, *Electrochim. Acta* 44 (1999) 4345–4356.
- [42] C.H. Hsu, F. Mansfeld, *Corrosion* 57 (2001) 747–748.
- [43] X. Wu, H. Ma, S. Chen, Z. Xu, A. Sui, *J. Electrochem. Soc.* 146 (1999) 1847–1853.
- [44] G.O. Mepes, J.M. Moore, *Handbook of Fuel Cell: Fundamentals, Technology, and Applications*, John Wiley and Sons, Ltd., New York, 2003, pp. 286–293.